Journal of Energy Storage 86 (2024) 111170

Contents lists available at ScienceDirect

Journal of Energy Storage

journal homepage: www.elsevier.com/locate/est

Research Papers

Performance analysis of a novel multi-module columnar packed bed reactor with salt hydrates for thermochemical heat storage

Changsheng Hao [a,1], Guosheng Feng [a], Changjie Ma [a], Camila Barreneche [b], Xiaohui She [a,*]

[a] School of Mechanical Engineering, Shijiazhuang Tiedao University, Shijiazhuang 050043, Hebei, China
[b] Department of Materials Science and Physical Chemistry, Universitat de Barcelona, Martí I Franqués 1, 08028 Barcelona, Spain

ARTICLE INFO

Keywords:
Salt hydrate
Thermochemical heat storage
Packed bed
Seasonal energy storage

ABSTRACT

The thermochemical heat storage based on salt hydrate has great advantages of high energy storage density and applicability to seasonal heat storage. In conventional packed-bed reactors, salt hydrates are often simply accumulated, and the air diffuses inside the pores. As a result, the salt hydrates are prone to agglomeration during the reaction, which will reduce the performance. To address these issues, this paper designs a multi-module columnar packed-bed reactor. The performance of top peripheral air intake and bottom central air intake schemes is numerically compared, and the effects of working parameters, structural parameters and physical parameters are analyzed. The results show that the bottom central air intake scheme has obvious advantages of uniform reaction rate, short reaction time and small resistance loss compared with the top peripheral air intake scheme. It is found that the reaction time is shortened by 46.6 % and the heat storage efficiency increases from 80.4 % to 83.8 % when the inlet air temperature increases from 75 to 95 °C. Besides, the reaction time decreases by 20.7 % as the inlet air velocity increased from 1 to 3 m/s and the optimal spacing of the hydrated salt modules is 0.3 cm. These results are promoting the development of thermochemical heat storage.

1. Introduction

Proportionally with the rapid development of modern society, the requirement for energy is increasing day by day, resulting in the depletion of traditional fossil energy and the increasingly serious problem of greenhouse gas emissions [1–3]. To relieve the above issues, many countries have started to use renewable energy and announced their carbon neutrality goals [4]. The proportion of renewable energy in the global energy production structure will increase from 15 % in 2020 to about 56 % in 2050 [5–7]. However, renewable energy faces a mismatch between supply and demand because of their intermittency and space dependency [8]. The thermal energy storage technology is an effective way to realize the efficient application of renewable energy [9] among which thermochemical heat storage (TCHS) has the largest theoretical energy density (>1GJ/m^3). In addition, the heat loss can be almost negligible during storage period by providing an excellent solution for seasonal heat storage with the advantages of being more compact and efficient [10,11].

Salt hydrates have attracted widespread attention due to their low cost and low environmental impact characteristics when considering medium or low temperature applications [12]. The salt hydrate based TCHS undergoes three processes of heat charging (endothermic dehydration), heat storage, and heat discharging (exothermic hydration), as shown in Fig. 1. The thermochemical reaction of salt hydrates can be described as follows:

$$Salt{\cdot}(x+y)H_2O_{(s)} + Q \underset{Discharging}{\overset{Charging}{\longleftrightarrow}} Salt{\cdot}xH_2O_{(s)} + yH_2O_{(g)} \quad (1)$$

The thermochemical reactor is a key component in the TCHS system, whose structural parameters, types and operating parameters affect the system performance. Thus, it is necessary to optimize the parameters of the reactors [13–15]. The commonly used reactors include packed bed reactor, moving bed reactor, and multi-module reactor [16], as shown in Fig. 2. Packed bed reactor is mostly cylindrical structure, with solid particles arranged in containers to react with the adsorbents flowing through them. It is easier to modeling due to the reduced system complexity [17]. A.A. Hawwash et al. [15] studied the heat storage performance of $MgCl_2$ in convergent truncated cones reactors with different ratios of inlet to outlet area and found that reactors with lower area ratios had shorter heat storage time and higher pressure drop and temperature difference. Maximum variation of the energy storage of the

* Corresponding author.
E-mail address: shexh19@hotmail.com (X. She).
[1] First author at: School of Mechanical Engineering, Shijiazhuang Tiedao University, Shijiazhuang 050043, Hebei, China.

https://doi.org/10.1016/j.est.2024.111170
Received 19 September 2023; Received in revised form 6 February 2024; Accepted 28 February 2024
Available online 6 March 2024

Nomenclatures

A_f	pre-exponential Arrhenius factor, 1/s
C_p	specific heat capacity, J/(kg•K)
c	molar concentration, mol/m^3
D_g	gas diffusivity in porous reactive bed, m^2/s
E_a	Arrhenius activation energy, kJ/mol
H	height of the reactor, cm
ΔH_r	reaction enthalpy, kJ/mol
h	convective heat transfer coefficient, W/(m^2•K)
k	permeability of the reaction salt bed, m^2
L	width of the salt hydration module section, cm
L_2	spacing of the salt hydration module, cm
M_s	molecular mass of salt, g/mol
M_v	molecular mass of vapor (g•mol^{-1})
n_b	number of moles of inorganic salts
P	Power, W
P_{eq}	equilibrium pressure, Pa
P_{ref}	reference pressure, 1 bar
P_v	partial pressure of water vapor
$\vec{P}_v$	water vapor pressure vector
R	universal gas constant, J/(mol•K)
r_0	radius of the bottom pipe, cm
r_1	external radius of hydrated salt module, cm
r_2	upper channel width, cm
Re	Reynolds number
ΔS_r	reaction entropy, J/(mol•K)
$\dot{S}_v$	water vapor mass source term, kg/(m^3•s)
$\dot{S}_q$	energy source term, W/m^3
t	Time, min
T	Temperature, K
T_{eq}	equilibrium temperature, K
$\vec{u}$	local velocity, m/s
W	height of the salt hydration module section, cm

Greek symbols

α	conversion rate of the local area of the salt bed
ε	porosity
η	thermal efficiency
λ	thermal conductivity, W/(m•K)
μ_w	dynamic viscosity of wet air, kg/(m•s)
ρ	Density, kg/m^3
ϕ	stoichiometric number

Subscripts

0	hydrated salt
ch	charging
eff	effective
f	dehydrated salt
gas	gas
in	inlet
loss	dissipate
out	outlet
ref	reference
s	solid salt
s_0	solid reactants
s_1	solid reaction products
sen	sensible
sto	store
tim	thermal insulating material
v	water vapor
w	wet air

Abbreviations

ESD	energy storage density
TCHS	thermochemical heat storage
TCM	thermochemical materials

thermochemical material is about 25.5 % and the dehydration time more than three times due to design reactor changing. Li et al. [18] cascaded reaction subunits filled with different thermochemical materials (TCM) to form an integrated packed bed, thus improving the output performance. The results indicate that the maximum temperature difference between the heat transfer fluid and the solid reactant was 3.5–4.9 °C during the charging process. However, poor heat and mass transfer occurs due to the limited contact area within the packed bed reactors, which leads to large pressure losses, resulting in an uneven reaction prone to agglomeration and deliquescence.

To avoid the drawbacks of packed bed reactors, researchers try to use moving bed reactors or radial flow reactor. Aldo Cosquillo Mejia et al. [19] demonstrated the feasibility of a moving bed reactor for TCHS through experiments. The authors flowed composite TCM (CaO particles and $Ca(OH)_2$ particles coated with Al_2O_3 nanostructure particles) through the tubes only with the help of gravity, and the heat exchange fluid flowed on the shell side of the reactor guided by baffles. The results show that the reaction performance, cyclic stability, and flow ability of the reactor were satisfactory. Lauren Farcot et al. [20] investigated a moving-bed thermochemical reactor with hydrated salt and humid air flow, suitable for building heating applications. The author tested the performance of $SrBr_2$•H_2O/$SrBr_2$•$6H_2O$ pair in the reactor and demonstrated the feasibility of the reactor. However, the moving bed reactors have complex hydrodynamics and modeling [21,22], and require moving parts which will create additional difficulties during the design phase. In addition, the mechanical strength and chemical stability requirements for TCM are relatively high. Pujari et al. [23] evaluated the performance of the vertical cylindrical annular reactor configuration, considering innovative radial airflow configurations. The detailed study of inward and outward radial flow configurations exhibited that the reactor performance significantly depended on the flow work requirement. They believed that the pressure drops and the ratio of the energy stored (or extracted) to the flow work were required to serve as crucial performance metrics.

Increased flow channel and contact area of adsorbate can enhance heat and mass transfer [24] in a multi-module reactor. Benoit Michel et al. [25] designed a layered modular reactor, using $SrBr_2$ as a TCM for several months of experiments to simulate seasonal heat storage, and achieved a ESD of 203kWh/m^3 and heat release power of 0.75-2 W/kg. Mass transfer is significantly improved due to the existing diffusion paths between adjacent modules. The authors stated that the reactor bed structure was a key factor that needed to be thoroughly analyzed and further developed to improve the performance of system. Moreover, Stengler et al. [26] designed a lab-scale reaction bed consisting of two units, and each unit was segmented into multiple sub-regions by branched fins; the heat transfer fluid flowed through the central tube and exchanged heat with the heat storage material surrounding the tube. The energy storage density (ESD) of the system is enhanced due to the topology optimization of the storage unit. Honeycomb heat exchanger is another form of modular reactor. K. Kant et al. [27] filled K_2CO_3 into a honeycomb reactor, and the TCM and the heat transfer fluid exchanged heat indirectly through the wall. The authors discovered that reducing the unit size of the honeycomb heat exchanger provides better heat transfer performance and faster reaction rate to a certain level.

In summary, the multi-module reactor can enhance the heat and mass transfer capacity, and also prevent common problems such as

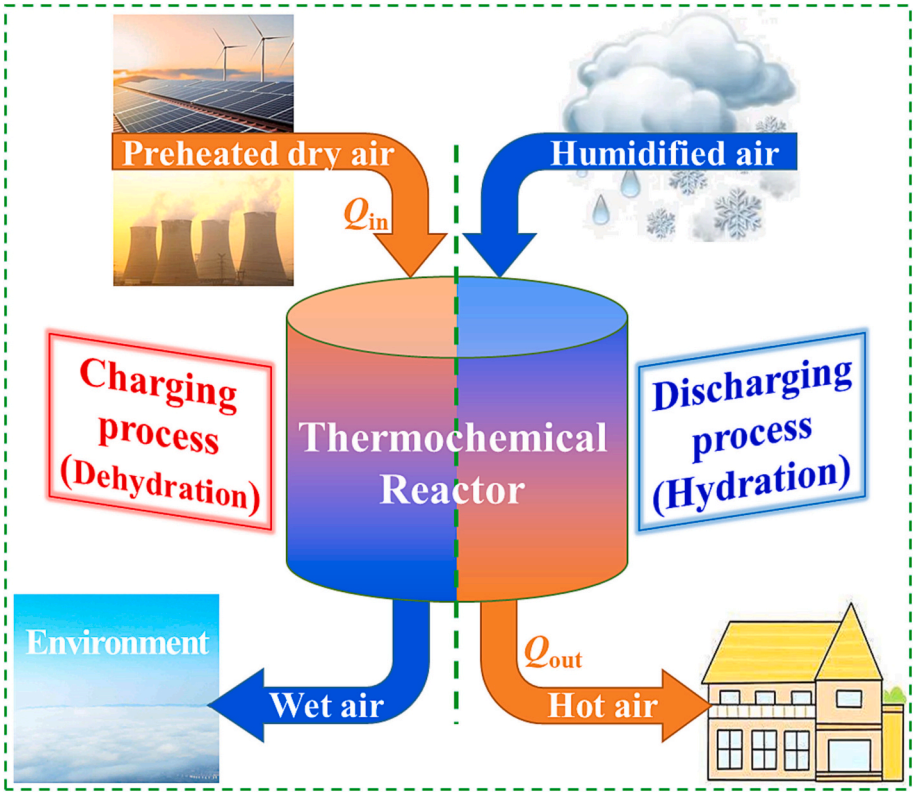

Fig. 1. Schematic diagram of the salt hydrate based TCHS system.

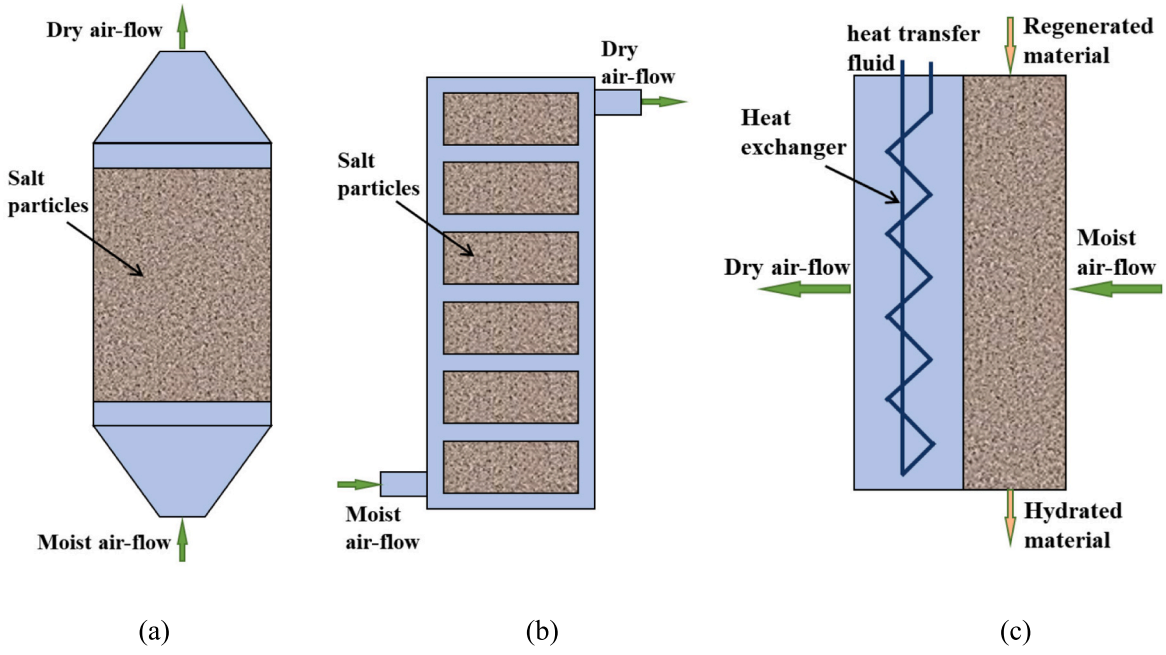

Fig. 2. Schematic of the (a) packed bed reactor; (b) multi-module packed bed reactor; (c) moving bed reactor.

agglomeration and deliquescence caused by uneven reaction. However, the research on the multi-module reactor is very limited. There have no reports on the compact cylindrical structure in the design of multi-module reactors used for salt hydrate based thermochemical thermal storage systems so far. Correspondingly, there have no detailed evaluation of the impact of various design aspects. So further in-depth research on the multi-module reactors is needed. In this paper, a novel columnar packed bed with multi-module is designed as an open reactor, which increases the contact area between reactants resulting in a more uniform reaction. The heat storage performance of the reactor is numerically studied with different air intake schemes. The influence of working parameters, structural parameters and physical property parameters is further analyzed, providing useful guidance for the application of TCHS systems.

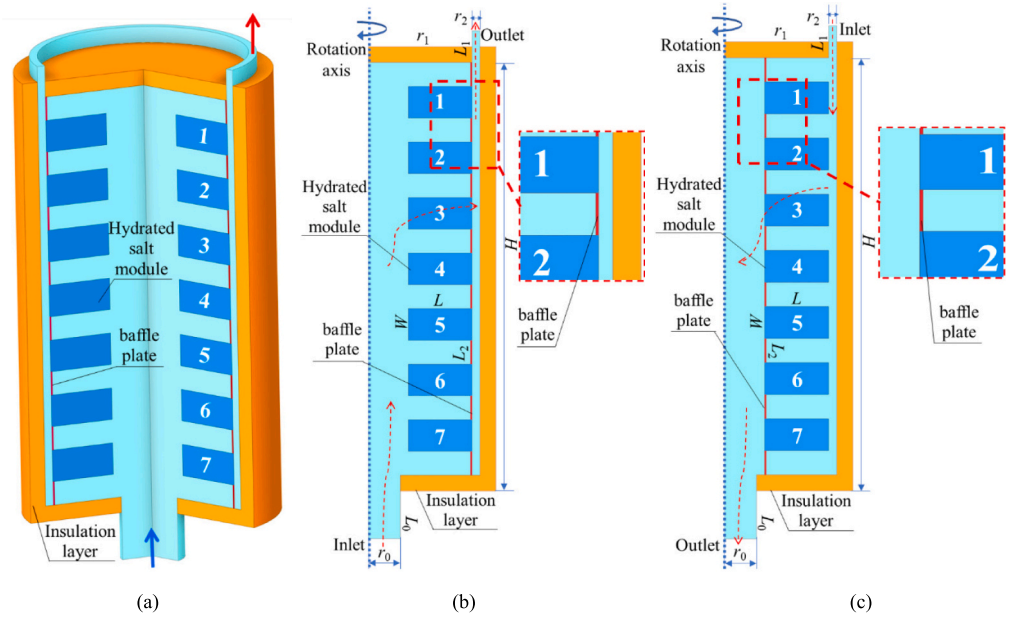

Fig. 3. Schematic diagram of reactor structure: (a) 3D cross-sectional view of bottom central air intake scheme; (b) bottom central air intake scheme; (c) top peripheral air intake scheme.

Table 1
Reactor structural parameters.

Parameters	Value
Radius of the bottom pipe r_0 (cm)	2
External radius of hydrated salt module r_1 (cm)	6.5
Upper channel width r_2 (cm)	0.5
Height of the reactor H (cm)	26
Spacing of the salt hydration module L_2 (cm)	1.5
Width of the salt hydration module section L (cm)	4
Height of the salt hydration module section W (cm)	2
Thickness of the insulation material (cm)	1

2. Mathematical model of multi-module columnar packed bed reactor

In this paper, $SrBr_2{\bullet}H_2O$ is selected as the TCM due to its excellent heat storage performance [10,17,24,28–30]. $SrBr_2{\bullet}6H_2O$ is heated by renewable energy such as solar energy and industrial waste heat for a dehydration reaction, and the thermal energy is converted into chemical potential and stored in $SrBr_2{\bullet}H_2O$. When heating is required, water vapor is brought into contact with $SrBr_2{\bullet}H_2O$ to undergo exothermic reaction. The reversible thermochemical reaction process is described by the Eq. (2) [31,32]:

$$SrBr_2{\cdot}6H_2O_{(s)} + 5\Delta H_r \underset{Discharging}{\overset{Charging}{\longleftrightarrow}} SrBr_2{\cdot}H_2O_{(s)} + 5H_2O_{(g)} \quad \Delta H_r = 67400\text{J} \Big/ \text{mol} \tag{2}$$

Literature research reveals a limited studies on hydrate salt reactors used in open thermal energy storage systems. As concluded in reference [33], the enhancement of heat and mass transfer and compactness are two crucial factors to consider when designing the reactor. Therefore, further in-depth research is necessary for the reactor used in open systems. This paper proposes a reactor with multiple modules, dividing the reactor structure into several modules based on the packed bed reactor, and its structure and size are shown in Fig. 3. Seven ring-shaped columnar salt hydrate modules wrapped with metal mesh are evenly arranged inside the reactor. The center of the lower part is connected to a round pipe, and the upper shell is provided with annular flow channels, which serve as air inlet or outlet.

The surfaces are wrapped with insulating material to reduce heat loss. The advantage of this improvement lies in the fact that the reaction gas flow and the stratified reaction bed can achieve heat exchange in three directions: the upper and lower surfaces, as well as the internal side surfaces. Additionally, it can promptly discharge the water vapor generated during the heat storage process, thereby improving the adsorption/desorption process of the hydrate salt. Table 1 lists the parameters related to the reactor. Due to the smaller size of each reaction module, adverse phenomena such as hindered heat and mass transfer during the actual reaction process can be effectively avoided. Two air flow modes are considered: bottom center air intake scheme and top peripheral air intake scheme, as show in Fig. 3(b) and (c). In Fig. 3, the identification numbers of each salt block are also marked. It is worth noting that the volume of the baffle plates in bottom central air intake scheme is larger than that in top peripheral air intake scheme.

2.1. Numerical model

2.1.1. Governing eqs.

1) Assumptions

The secondary influencing factors are ignored to simplify the calculation, the following assumptions are made [33–36]:

(1) The gas is viewed as an ideal gas which is composed of dry air and water vapor.
(2) The gas flow rate in the porous media follows Brinkman-Forchheimer extended Darcy's law.
(3) Ignoring the influence of radiation.
(4) The zone with packed salt particles is treated as a porous media material area. The particle accumulation in the reaction bed is uniform, and the porosity is uniform in space;
(5) The pores of the metal mesh are sufficient for the gas flow to pass through, and have no effect on the flow;
(6) The local thermal equilibrium hypothesis between the gas and solid in the porous bed is implemented due to the small gas velocity inside the porous;
(7) The reaction enthalpy ΔH_r is regarded as a constant.

2) Reaction kinetic equations

According to the literature [37–39], the reaction kinetics is related to three major variables: reaction conversion rate α, water vapor partial pressure P_v and temperature T. The reaction rate is defined as follows:

$$\frac{\partial \alpha}{\partial t} = A_f \cdot exp\left(-\frac{E_a}{RT}\right)\cdot(1-\alpha)\cdot\left(1-\frac{P_v}{P_{eq}}\right) \tag{3}$$

$$\vec{u} = -\frac{k}{\mu_w}\nabla P \tag{9}$$

Brinkman's equation:

$$\frac{\partial}{\partial t}(\varepsilon\rho_w) + \nabla(\rho_w \vec{u}) = \dot{S}_v \tag{10}$$

$$\frac{\partial}{\partial t}(\rho_w \vec{u}) + \left(\frac{\vec{u}}{\varepsilon}\nabla\right)(\rho_w \vec{u}) = \nabla\left[-\varepsilon\vec{P}_v I + \mu_w\left(\nabla\vec{u} + (\nabla\vec{u})^T\right) - \frac{2}{3}\mu_w(\nabla\vec{u})I\right] + \dot{S}_v\frac{\vec{u}}{\varepsilon} - \varepsilon\frac{\mu_w}{k}\vec{u} \tag{11}$$

where α is the conversion rate of solid reactants converted into products, defined as $\alpha = \frac{n_0 - n}{n_0}$ (where n_0 and n represent the moles of the solid reactant at initial time and at time t); and A_f represents the pre-exponential Arrhenius factor (1/s); E_a represents the Arrhenius activation energy; R represents the universal gas constant; P_v represents partial pressure of water vapor in the local area; P_{eq} represents the pressure when water vapor reaches reaction equilibrium at temperature T.

In the solid-gas chemical reaction, the equilibrium pressure P_{eq} and temperature T_{eq} satisfy the Clausius-Clapeyron equation [40,41]:

$$ln\left(\frac{P_{eq}}{P_{ref}}\right) = -\frac{\Delta H_r}{\phi R T_{eq}} + \frac{\Delta S_r}{\phi R} \tag{4}$$

where P_{ref} represents the reference pressure (1 bar); ΔH_r represents the reaction enthalpy (kJ/mol); ΔS_r represents the reaction entropy (J/mol); and ϕ represents the stoichiometric number.

3) Continuity conservation equation

The charging process of hydrated salt includes the density change process of hydrated salt and water vapor. The governing equations are expressed as:

$$(1-\varepsilon)\frac{\partial \rho_s}{\partial t} = \rho_s \frac{\partial \alpha}{\partial t} \tag{5}$$

$$\varepsilon\frac{\partial \rho_v}{\partial t} = \dot{S}_v - \nabla(\rho_v \vec{u}) + D_g \Delta \rho_v \tag{6}$$

where ε is the porosity of the salt bed; ρ_v and ρ_s represent the density of water vapor and salt bed respectively; D_g is the diffusion coefficient of water vapor; $\dot{S}_v$ represents the water vapor mass source term, which is related to the concentration of the solid reactant and reaction rate, and it can be expressed as:

$$\dot{S}_v = \phi c_s \frac{\partial \alpha}{\partial t} \tag{7}$$

Where c_s represents the molar concentration of the salt bed, and ϕ is the stoichiometric number.

4) Momentum conservation equation

The momentum conservation characteristics of the porous media region are generally described based on Darcy's law or Brinkman's equation, which are expressed as follows:

Darcy's law:

$$\frac{\partial}{\partial t}(\varepsilon\rho_w) + \nabla(\rho_w \vec{u}) = \dot{S}_v \tag{8}$$

where ρ_w is the density of wet air; $\vec{u}$ is the velocity vector of wet air; $\vec{P}_v$ is the water vapor pressure vector; μ_w represents the dynamic viscosity of wet air (kg/(m•s)); k is the permeability of the reaction salt bed (m^2), and the superscript T represents turbulence.

Darcy's law describes the law of the linear relationship between the seepage velocity and the pressure drop of the gas flow in porous media, which is suitable for slow laminar flow with $Re < 1$. Brinkman's equation describes the phenomenon of rapid fluid flow (still in laminar flow state) with $Re > 1$ in porous media, and considers the influence of shear energy dissipation [15,42]. Seepage will be excessively irregular and mixed with each other.

5) Energy conservation equation

The energy conservation equation can be expressed as:

$$(\rho C_p)_{eff}\frac{\partial T}{\partial t} + C_{p,v}\rho_v \vec{u}\nabla T = \nabla(\lambda_{eff}\nabla T) + \dot{S}_q \tag{12}$$

where C_p represents the specific heat capacity; λ represents the thermal conductivity; and $\dot{S}_q$ represents the energy source term. Where $(\rho C_p)_{eff} = (1-\varepsilon)(\rho C_p)_s + \varepsilon(\rho C_p)_v$, and the subscripts s and v represent the salt bed and gas, respectively. The effective thermal conductivity of the reaction bed is expressed as $\lambda_{eff} = (1-\varepsilon)\lambda_s + \varepsilon\lambda_v$.

The physical parameters of the salt bed are related to the conversion rate during charging, and can be expressed as:

$$(\rho C_p)_s = (1-\alpha)(\rho C_p)_{s0} + \alpha(\rho C_p)_{s1} \tag{13}$$

$$\lambda_s = (1-\alpha)\lambda_{s0} + \alpha\lambda_{s1} \tag{14}$$

where the subscripts s_0 and s_1 represent solid reactants and products, respectively.

The energy source term represents the heat absorbed or released during the reaction process, expressed as:

$$\dot{S}_q = \pm c_s \frac{\partial \alpha}{\partial t}\Delta H_r \tag{15}$$

where the sign ± depends whether it is hydration or dehydration.

2.1.2. Initial and boundary conditions

Variables like temperature, pressure, conversion rate, flow rate, and concentration are related to time and space and can be written as $T(t,x,y,z)$, $P(t,x,y,z)$, $a(t,x,y,z)$, $\vec{u}(t,x,y,z)$, and $c(t,x,y,z)$ in the reactor. The initial water vapor concentration, which is calculated using the Clausius-Clapeyron equation under the initial temperature condition inferred, is uniformly distributed inside the reactor. In addition, the temperature, pressure, conversion rate, and gas flow rate inside the reactor are

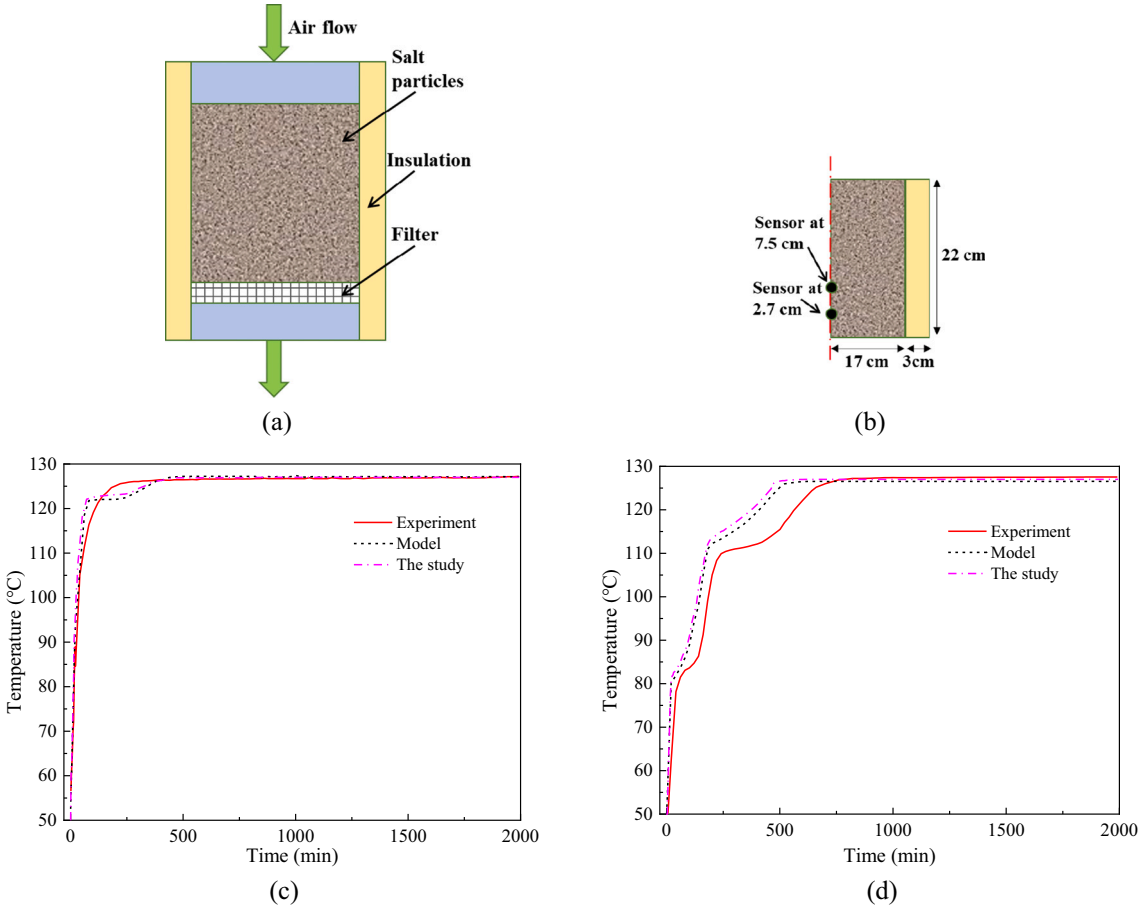

Fig. 4. Comparison of experimental and numerical calculation results: (a) Schematic diagram of cylindrical packed bed; (b) Model geometry of packed bed; (c) Sensor at 2.7 cm; (d) Sensor at 7.5 cm.

considered to be consistent with the environment at the beginning of the charging process. The initial conditions of the above parameters can be expressed as:

$$T(0,x,y,z)=T_0; P(0,x,y,z)=P_{ref}; a(0,x,y,z)=0;\quad \vec{u}(0,x,y,z)=0; c(0,x,y,z)=c_0 \tag{16}$$

The temperature, velocity, and water vapor partial pressure of the hot air intake are constant at the inlet:

$$T=T_{in};\quad \vec{u}=u_{in}; P_v=P_{v0} \tag{17}$$

Natural convection heat transmission takes place between the reactor's outside surfaces and the surrounding air despite being covered in insulation. As stated in the boundary condition equation:

$$\lambda\frac{\partial T}{\partial x}=h\left(T_w-T_f\right), \nabla\vec{u}=0 \tag{18}$$

The temperature gradient is zero and the pressure is equal to ambient pressure at the output, which is written as:

$$\lambda\frac{\partial T}{\partial z}=0; P=P_{ref} \tag{19}$$

Table 2
The relationship between evaluation indicators and the quantity of grids.

Grid scheme	Quantity of grids	Velocity (m/s)	Change rate of velocity $(v_n\text{-}v_{n\text{-}1})/v_{n\text{-}1}$	The average temperature (°C)	Change rate of temperature $(T_n\text{-}T_{n\text{-}1})/v_{n\text{-}1}$	Reaction time (min)	Change rate of reaction time $(\Delta t_n\text{-}\Delta t_{n\text{-}1})/\Delta t_{n\text{-}1}$
Extremely coarse	3411	0.0127	/	83.56	/	1248.1	/
Coarser	4756	0.0130	2.4 %	83.57	0.01 %	1326.5	6.28 %
Normal	9134	0.0131	1.2 %	83.55	−0.02 %	1360.7	2.58 %
Finer	18,616	0.0135	2.7 %	83.52	−0.04 %	1373.5	0.94 %
Extra fine	43,977	0.0138	2.1 %	83.51	−0.01 %	1378.8	0.39 %
Extremely fine	116,096	0.0139	0.95 %	83.50	−0.01 %	1377.6	−0.09 %

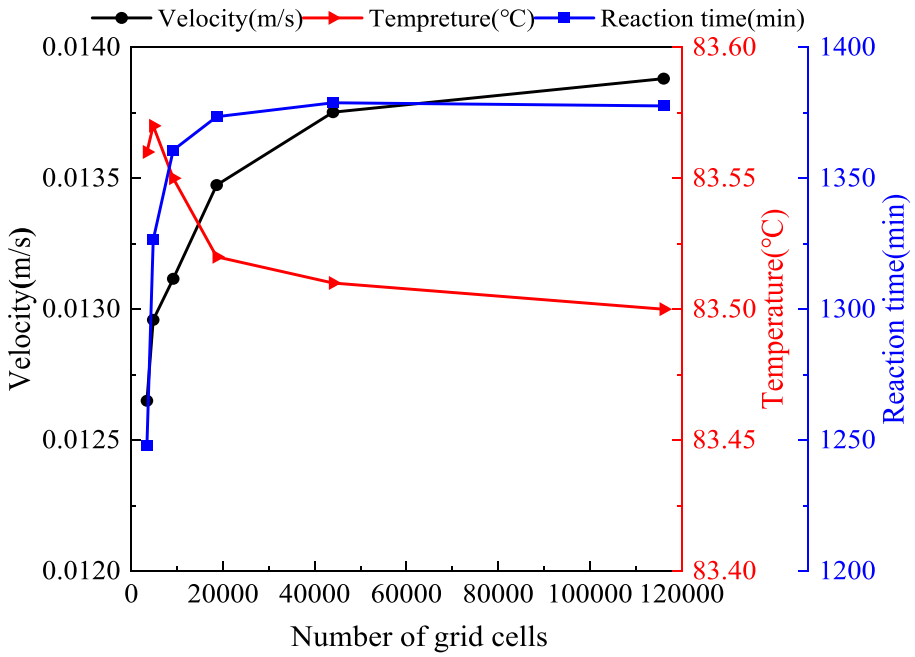

Fig. 5. Grid independence verification results.

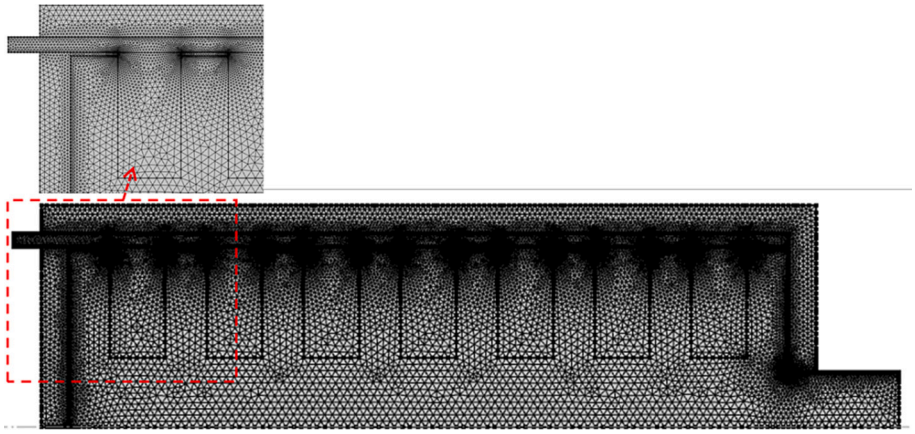

Fig. 6. Reactor grid.

2.2. Computational algorithm and model validation

The experiment carried by A. Rubino et al. [42,43] from the Netherlands Energy Research Center is used to validate the accuracy of the numerical model. The experimental platform consists of a cylindrical shell with TCM ($MgCl_2{\cdot}6H_2O$) within, and the shell has ports for admission and outflow at each end. In this work, the dehydration process was modelled and computed. Preheated dry air at 401 K enters from

Table 3
The properties of TCHS system used in numerical simulation.

Parameter	Description	Value	Parameter	Description	Value
M_v	Molecular mass of vapor (g•mol^{-1})	18.02	$T_{in,\ ch}$	Input temperature of charging (°C)	85
M_{s1}	Molecular mass of $SrBr_2$•$6H_2O$ (g•mol^{-1})	355.49	$T_{0,\ ch}$	Environment temperature in charging (°C)	30
M_{s0}	Molecular mass of $SrBr_2$•H_2O (g•mol^{-1})	265.44	p_{ref}	Reference pressure (Pa)	101,325
C_{ps1}	Specific heat of $SrBr_2$•$6H_2O$ (J•kg^{-1}•K^{-1})	967	P_0	Partial pressure of water vapor (Pa)	600
C_{ps0}	Specific heat of $SrBr_2$•H_2O (J•kg^{-1}•K^{-1})	456	D_g	Gas diffusion coefficient (m^2•s^{-1})	$2.82{\cdot}10^{-5}$
C_{tim}	Specific heat of thermal insulating material (J •kg^{-1}•K^{-1})	1280	u_{in}	Velocity of inlet air (m•s^{-1})	2.5
λ_{s1}	Thermal conductivity of $SrBr_2$•$6H_2O$ (W•m^{-1} •K^{-1})	0.71	ε	Porosity	0.65
λ_{s0}	Thermal conductivity of $SrBr_2$•H_2O (W•m^{-1} •K^{-1})	0.56	A_f	Frequency factor in Arrhenius' equation (s^{-1})	16,300
λ_{tim}	Thermal conductivity of thermal insulating material (W•m^{-1}•K^{-1})	0.004	E_a	Activation energy (kJ•mol^{-1})	55
ρ_{s1}	Density of $SrBr_2$•$6H_2O$ (kg•m^{-3})	2390	R	Ideal gas constant (J•mol^{-1}•K^{-1})	8.314
ρ_{s0}	Density of $SrBr_2$•H_2O (kg•m^{-3})	3480	ΔH_r	Reaction enthalpy (kJ•mol^{-1})	337
ρ_{tim}	Density of thermal insulating material (kg•m^{-3})	240	ΔS_r	Reaction entropy (J•mol^{-1}•K^{-1})	875
k_{s1}	Permeability of $SrBr_2$•$6H_2O$ (m^2)	$3.1{\cdot}10^{-11}$	h	Convective heat transfer coefficient (W·m^{-2}•K^{-1})	4
k_{s0}	Permeability of $SrBr_2$•H_2O (m^2)	$0.7{\cdot}10^{-10}$	ϕ	stoichiometric number	5

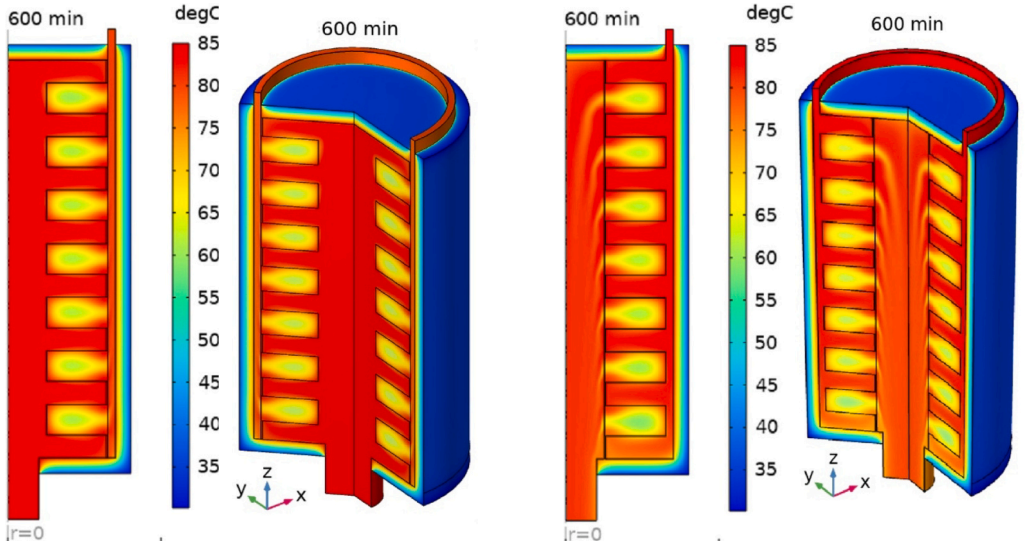

(a) bottom central air intake scheme **(b) top peripheral air intake scheme**

Fig. 7. The distribution of temperature on the reactor section at 600 min.

the top of the reactor during the dehydration process. Temperature variations at two positions (2.7 cm and 7.5 cm) along the central axis of the reactor are monitored, and the section diagram of reactor and numerical results were shown in Fig. 4. The temperature curves of the two monitoring points differ from the author's experimental and numerical calculation results because of the unknown pertinent physical parameters which can only be found by checking other literature. Overall, the simulation findings demonstrate that the model generates reliable predictions and may be applied to further investigation.

Both the reactor and the governing equations developed in this research are rotational axisymmetric in geometry. Therefore, the reactor can be simplified as a two-dimensional model, as shown in Fig. 3(b) and (c). The COMSOL software was used as the solution analysis tool due to the outstanding multi-physics coupling simulation performance. The wall's boundary layer is a quadrilateral grid, the computational domain is discretized into an unstructured grid, and the remaining important regions are separated into triangular grids automatically in accordance with the predetermined physical model. Grid independence needs to be validated in order to strike a compromise between the accuracy and computational effectiveness of the simulation findings. Six division schemes were chosen, each with a different grid number as shown in Table 2.

The evaluation indexes of grid independence are the average velocity, average temperature, and reaction time of the reaction bed. The average temperature, time, and velocity of the reaction bed at a conversion rate of 0.995 are chosen as the assessment index since the reaction conversion rate rises steadily over time and takes a while to reach 1. Fig. 5 depicts the correlation between each evaluation index and the number of grids, while Table 2 lists the findings of the grid independence analysis. Extra fine grids are adopted in this paper due to the calculation time of extremely fine meshes increases by three times through there is no significant difference between the calculation results of them. The mesh division results are shown in Fig. 6.

2.3. Operating conditions and performance indexes

2.3.1. Operating conditions

A numerical simulation investigation on the heat and mass transfer characteristics of the reactor during the charging process was conducted. Physical fields including chemical reactions, dilute substance flow in porous media, the Brinkman equation, and heat transfer in porous media were used to solve the heat and mass transfer and the reaction kinetics. The evolution of variables time-by-hour such as temperature, pressure, flow rate, concentration, and conversion rate inside the reactor can be determined. It is important to perform computations under the same input flow (or similar velocity) and temperature conditions in order to compare the performance of the two operating schemes. The pertinent parameters are displayed in Table 3.

2.3.2. Performance indexes

1) Thermal efficiency

The hydrated salts convert absorbed heat into chemical energy and sensible heat during the charging process. Simultaneously, the temperature of the reaction bed shell gradually increases to store some heat as sensible heat, while some heat is lost by convective heat exchange between the reactor surface and the surroundings. The thermal efficiency (η_{ch}) reflects the utilization rate of input heat, and is generally defined as the ratio of the energy stored in the reactor to the heat consumed, which can be expressed by the following formula:

$$\eta_{ch} = \frac{Q_{sto}}{Q_{ch}} \tag{20}$$

The temperature of the reactor is slowly reduced to the ambient temperature when used for long-term heat storage. Thereby, the heat storage can be calculated according to the heat absorbed by the reaction.

$$Q_{sto} = (1-\varepsilon) \times n_b \times \Delta H_r \tag{21}$$

where n_b represents the moles of TCM.

The energy differential between the entrance and outlet of the reactor can be used to calculate the consumed heat Q_{ch}, which is equal to the total of the stored heat Q_{sto}, the sensible heat Q_{sen}, and the dissipated heat Q_{loss}. Q_{ch} can be expressed as

$$Q_{ch} = Q_{sto} + Q_{sen} + Q_{loss} = Q_{in} - Q_{out} \tag{22}$$

The energy at the inlet and outlet is the enthalpy value of the airflow, which can be calculated using the following equation:

$$Q_{in} = C_{P,gas,in}\rho_{gas,in}f_{gas,in}v_{gas,in}\int_0^{t_{ch}}\left(T_{gas,in}\right)dt \tag{23}$$

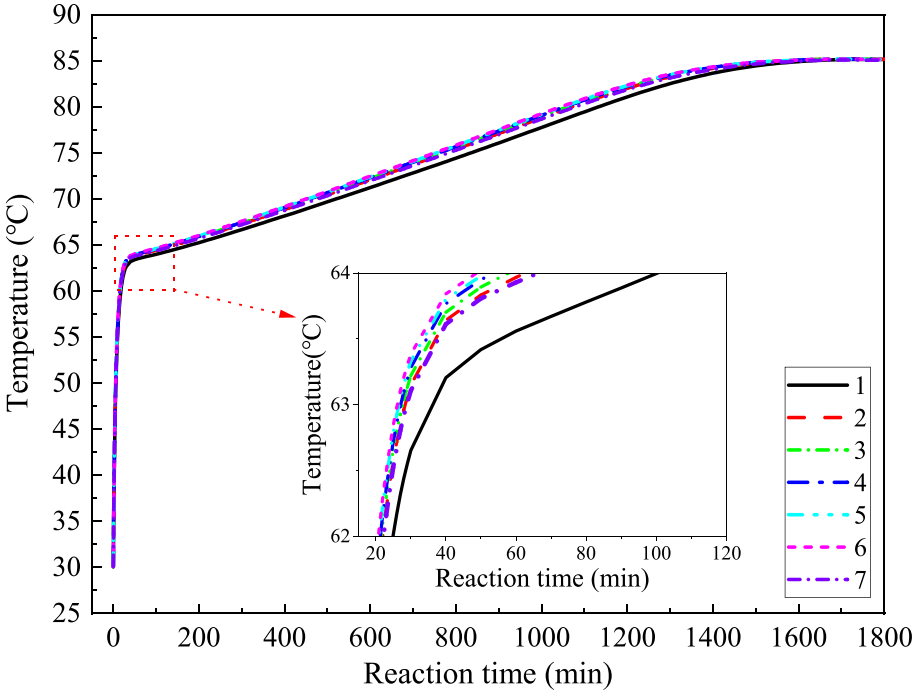

(a) bottom central air intake scheme

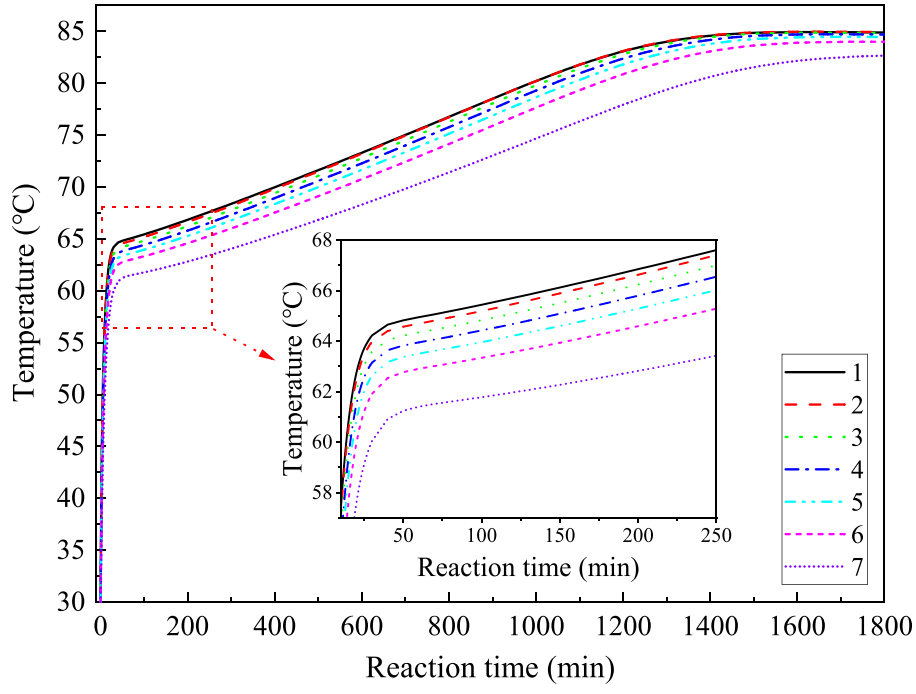

(b) top peripheral air intake scheme

Fig. 8. Time evolution of the average temperature of the salt hydrate units of reactor.

$$Q_{out} = C_{P,gas,out}\rho_{gas,out}f_{gas,out}v_{gas,out}\int_0^{t_{ch}}(T_{gas,out})dt \quad (24)$$

where $C_{p,\ gas,in}$, and $C_{p,gas,out}$ are the mass-specific heat of the gas flow at constant pressure. And f represents the cross-sectional area. The terms $v_{gas,in}$ and $v_{gas,\ out}$ are the average velocity of the gas flow in the inlet and outlet. The terms $T_{gas,in}$, and $T_{gas,out}$ denote the average temperature of the airflow at the inlet and outlet, respectively.

2) Heat power

The heat power P_{ch} denotes heat storage per unit time in the charging

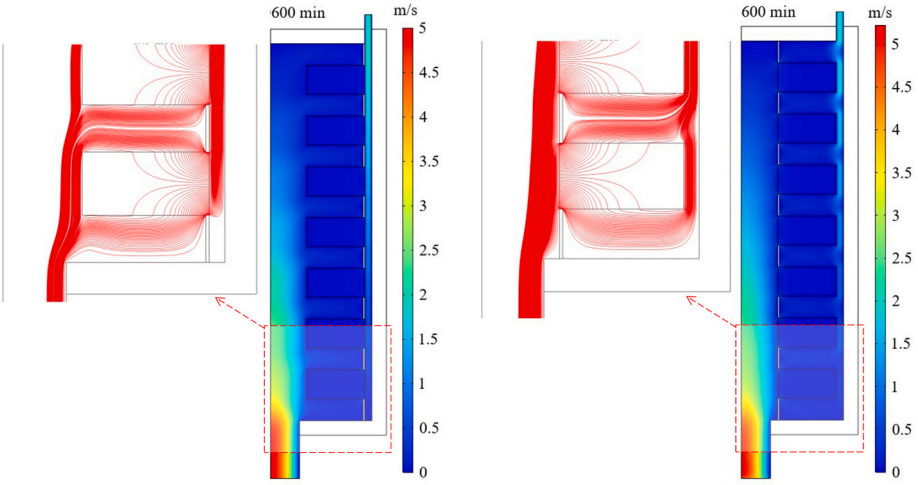

(a) bottom central air intake scheme (b) top peripheral air intake scheme

Fig. 9. The distribution of velocity and local streamline on the reactor section at 600 min.

process and can be expressed as:

$$P_{ch} = \frac{\partial \alpha}{\partial t} Q_{sto} \tag{25}$$

3) Energy storage density

The ESD is a crucial metric for determining the reactor's compactness. A higher ESD implies a small reactor volume, which is beneficial for miniaturization. Volume energy density (E_V) is used to express the ESD, and is expressed as

$$E_v = \frac{Q_{sto}}{V} \tag{26}$$

Where V represents the volume of the reactor (m^3).

4) Reaction time

The reaction time is defined as the dehydration time when the conversion rate is >99.5 %.

3. Results and discussion

3.1. Comparisons of reactor between bottom central air intake scheme and top peripheral air intake scheme

The reactor designed in this study considers two types of gas flow schemes, as bottom central air intake and top peripheral air intake. The performance indexes and reaction process consistency are necessary to be compared between them to determine the optimal intake scheme. During the charging process, air heated by solar energy or other energies flows in at a steady flow rate from the inlet. The desorption reaction occurs when the temperature of the salt bed reaches certain levels and the desorbed water molecules flow out of the reactor with the airflow.

3.1.1. Temperature profile of reactive bed and flow field of gas

Fig. 7 shows the temperature field distribution of the reactor at 600 min. It is discovered that the temperature fields of the two schemes are similar. The temperature in the edge of each salt module is higher than it in the core area, resulting in a higher reaction rate. This is because the airflow first undergoes an exothermic reaction in the edge area, resulting in a decrease in temperature after entering the central area. The hourly change of the average temperature of the seven circular column modules is depicted in Fig. 8. The temperature rises rapidly due to the large temperature difference between the air flow and the salt bed at first. Then, the dehydration reaction starts when the temperature reaches about 63 °C. The endothermic reaction causes the temperature to gradually increase until it reaches the inlet temperature after the reaction is finished.

Furthermore, Fig. 8 shows that the temperature change consistency of each salt module in the bottom central air intake scheme is superior to that of the top peripheral air intake scheme. Only the temperature curve of the salt module at the outflow of bottom central air intake deviates significantly from the other modules, while the temperature curves of the other modules are nearly identical. In the top peripheral air intake scheme, however, the farther away from the inlet, the lower the average temperature of the salt module. There is a significant difference between them which demonstrates that the reaction rate is influenced by the air flow field. This phenomenon is attributed to the reactor's unequal distribution of hot air. Most of the gas flow first reacts with the salt hydrate module in the upper part and processes the reaction. Therefore, the temperature of the gas flow entering the bottom part is low resulting in a lower reaction rate. It is worth noticing that the two salt modules at the bottom of the top peripheral air intake scheme have not yet achieved the inlet airflow temperature at 1800 min, indicating that the discharging process is still in progress. Because the gas flow is rather evenly distributed throughout the reactor in bottom central air intake scheme due to the broad inlet channel, the reaction rate of each hydrated salt module is almost the same.

Fig. 9 shows the flow field distribution in the reactor at 600 min. It shows that the hot air flow can fully and evenly reach each salt module because of the large flow channel in bottom central air intake's inlet section, resulting in a rather consistent response rate for each module. The flow velocity at the top of top peripheral air intake's inlet section is quite high, while the flow velocity at the bottom is comparatively low. Because of the small flow channel, the air flow first interacts with the upper salt module resulting in an unbalanced reaction.

3.1.2. Concentration profile of water vapor in reactive bed

Fig. 10 shows the hourly fluctuation in the average water vapor concentration of each salt module. Notice that the water vapor concentration grows rapidly at first and then falls slowly due to the decrease in reactant concentration. The concentration reduces to the inlet concentration value when the reaction is completed finally. The trend of change in water vapor concentration in each salt hydrate module of bottom central air intake scheme is essentially the same, however, it is

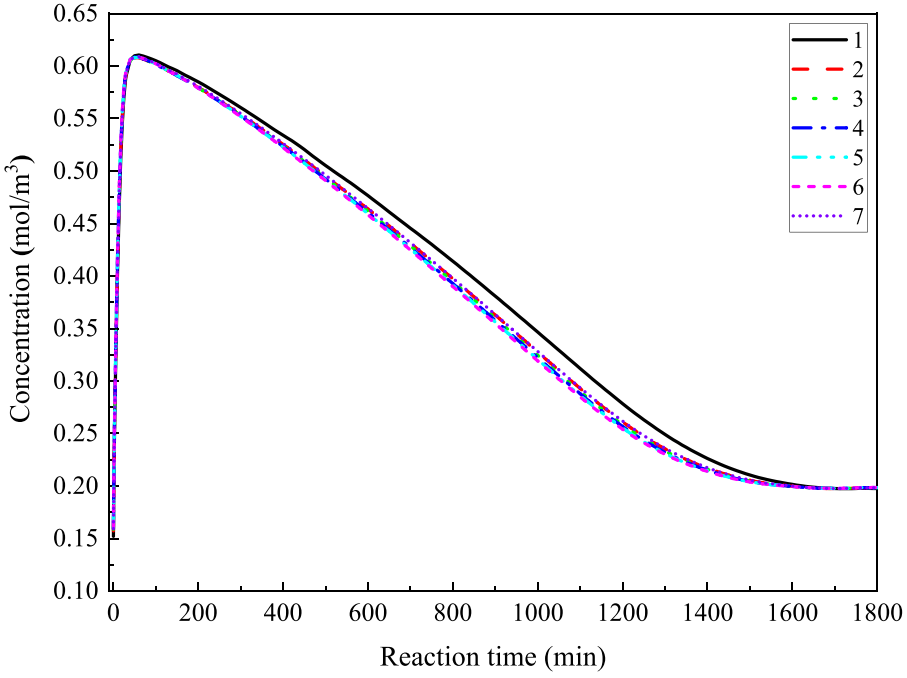

(a) bottom central air intake scheme

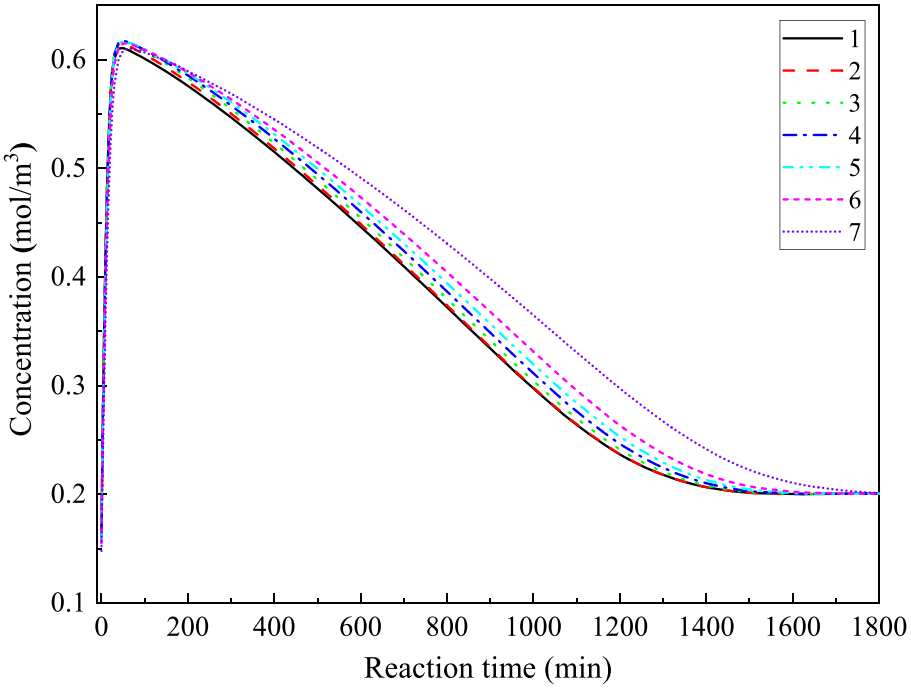

(b) top peripheral air intake scheme

Fig. 10. The average concentration of water vapor on the salt units of reactor over time.

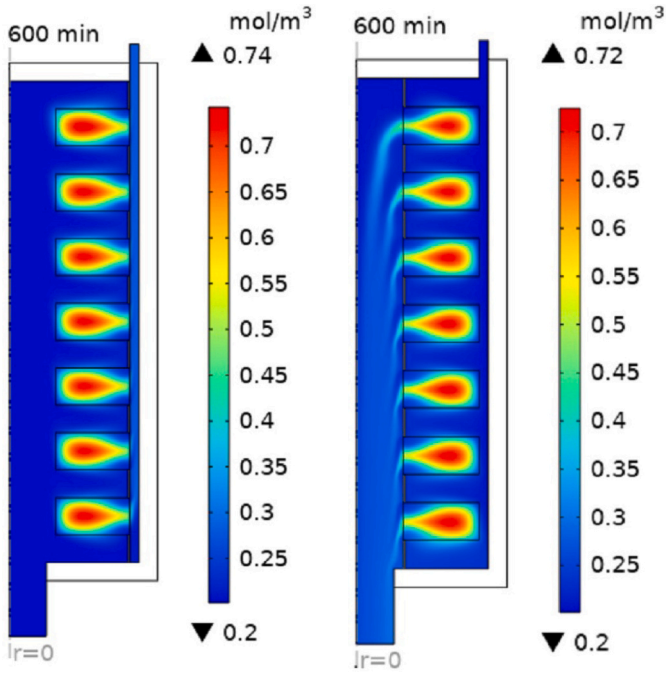

(a) bottom central air intake scheme (b) top peripheral air intake scheme

Fig. 11. The distribution of concentration on the reactor section at 600 min.

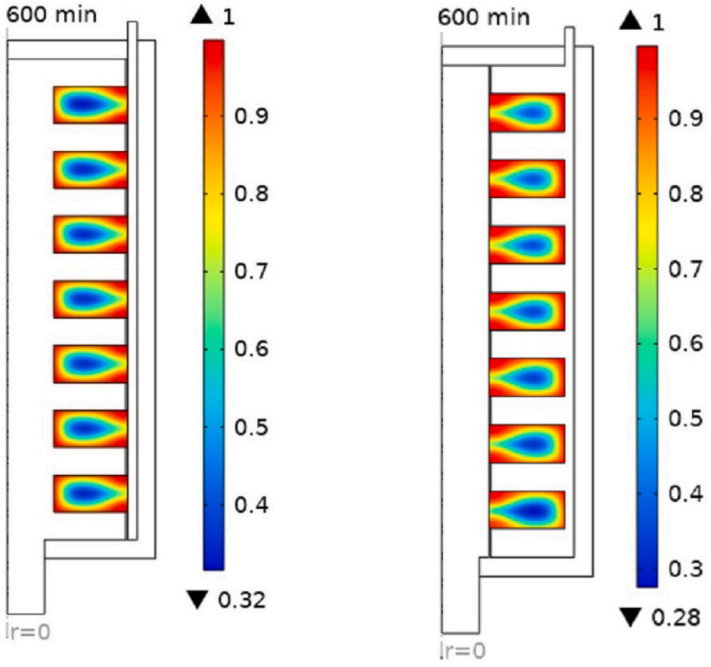

(a) bottom central air intake scheme (b) top peripheral air intake scheme

Fig. 12. The distribution of conversion rate on the reactor section at 600 min.

considerably different in top peripheral air intake scheme. The average concentration of the salt module farther from the intake is higher in the later reaction, indicating a slower reaction rate. Fig. 11 depicts the concentration distribution of the reactor's longitudinal section at 600 min. Notice that the concentration in the edge area is significantly lower than that in the center area, indicating that the conversion rate in the edge area is higher than that in the center area.

3.1.3. Conversion rate profile of reactive bed

The distribution of the conversion rate at 600 min is depicted in Fig. 12. The conversion rate gradually declines from the salt module's edge area to the interior area, and the region with a lower conversion rate (below 0.5) takes the form of droplets of water. It is obvious that the desorption reaction occurs gradually from the module's surface to the interior. Fig. 13 depicts the kinetics and conversion rate of each salt

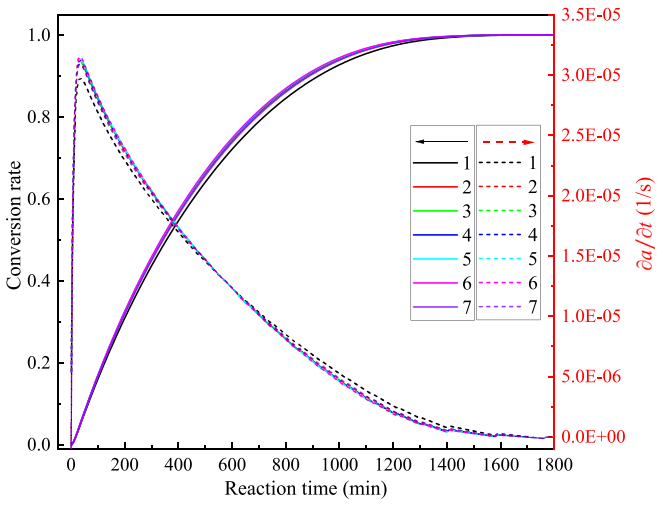

(a) bottom central air intake scheme

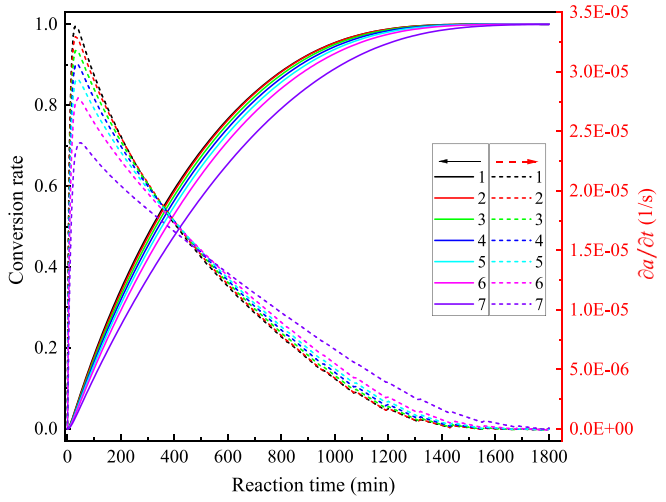

(b) top peripheral air intake scheme

Fig. 13. The average conversion rate and reaction kinetics on the salt units of reactor over time.

module over time. As can be observed, each salt module's conversion rate increases gradually over time. The main part of the salt has been dehydrated after 1200 min while the total reaction time is about 1600 min. The reaction rate rapidly increased to a maximum at the beginning and then decreased to zero until all hydrated salts were dehydrated.

Fig. 13 also shows that the reaction kinetics of each salt module in top peripheral air intake scheme differs significantly. The farther away from the inlet, the smaller the reaction kinetics, which is reflected in the large difference in conversion rate. In bottom central air intake scheme, the reaction kinetics and the conversion rate of each module are almost the same. It shows that the flow field distribution of this kind of open reactor has great influence on the dehydration process.

3.1.4. Resistance loss

Generally, the outlet of an open reactor is ambient and the pressure remains constant. The resistance loss of the reactor is affected by the constant changes in the temperature and composition of the gas flow. So, the inlet pressure must vary with resistance loss to maintain a constant inlet flow (velocity). Therefore, the resistance loss with the reaction process is analyzed to provide technical support for the selection of fan and the operating conditions.

The pressure distribution in the reactor's longitudinal section at 600 min is shown in Fig. 14. It is clear that the local resistance loss of the salt module makes up the majority of the reactor's resistance loss. The hourly evolution of the gauge pressure at the reactor inlet is depicted in Fig. 15. It can be seen that the internal pressure loss of the reactor rises rapidly at the initial stage of the dehydration reaction and then rapidly decreases to an unchanged value after reaching the peak value. One of the reasons is that the gas expansion due to the high-temperature gas flow enters. And the other is that the flow generates resistance. According to the study, the maximum resistance loss of bottom central air intake scheme peaks at 1008.7 Pa before stabilizing at about 471.5 Pa, while top peripheral air intake scheme peaks at 2308.9 Pa before stabilizing at about 1078.8 Pa. Obviously, the latter requires roughly 56.3 % less power than the former in terms of resistance loss, which lowers operating power consumption and boosts the charging performance of the system.

3.1.5. Performance index

The performance indexes include heat storage efficiency, heat storage power, ESD and reaction time, all of which reflect the performance characteristics of the system. Both the two schemes have the same ESD (75.1 kW•h/m^3) due to the same hydrated salt module and working parameters. The reaction times of bottom central air intake scheme and top peripheral air intake scheme are 1365.7 min and 1378.8 min, respectively. The reaction time of the bottom central air intake scheme is less than that of the top peripheral air intake scheme due to the uniform airflow.

The result shows that the heat storage efficiency of the bottom central air intake scheme is 82.2 %, as well as 81.7 % for the top peripheral air intake scheme. This is because the bottom central air intake scheme has a shorter reaction time and less heat loss than the top peripheral air intake scheme. The small amount of sensible heat obtained by the reactor shell is ignored in the calculation of heat storage efficiency. Fig. 16 shows the hourly variation of the heat storage power of the reactor under the two schemes. It can be shown that the heat storage power under the two schemes exhibits consistent hourly variation characteristics. It increases quickly to the peak value at the beginning of the instant, reaching 49.6 W and 48.2 W, respectively. Then it progressively drops to 0 W until the reaction is complete. The heat storage power is relatively high at the beginning due to the fairly homogeneous reaction kinetics for the bottom central air intake scheme. The reaction of the remaining hydrated salt slows down after 375 min as a result of the high conversion rate, and the heat storage power becomes marginally less than that of the top peripheral air intake scheme.

Compared with the top peripheral air intake scheme, the reaction rate of each module is relatively consistent, the reaction conversion rate is uniform, and the parameters such as temperature, water vapor concentration, and performance indicators have almost the same distribution under the bottom central air intake scheme. Bottom central air intake scheme also has the lower resistance loss. Therefore, the bottom central air intake scheme is selected for research in the following article.

3.2. Parametric study of reactor with bottom central air intake scheme

The structural parameters and working parameters of the reactor affect the charging performance. So, it is necessary to further study the performance of the reactor under different parameters. The following is to study the working performance of the bottom central air intake scheme under different inlet parameters (temperature, velocity, relative humidity), structural parameters (module spacing), physical properties (porosity, thermal conductivity), and other conditions, to seek reasonable working parameters to bring out the best performance.

3.2.1. The influence of inlet parameters

According to formula (3), increasing the temperature and velocity (equivalent to the flow rate) of the inlet airflow can improve the

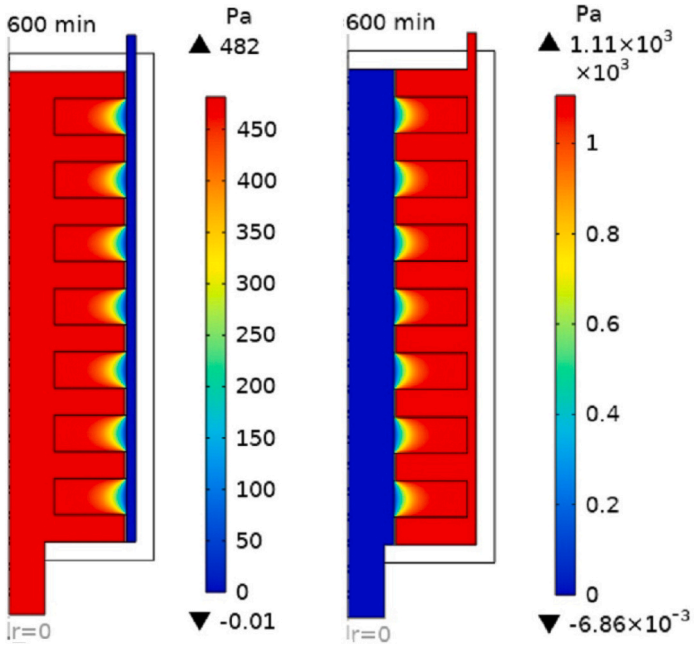

(a) bottom central air intake scheme (b) top peripheral air intake scheme

Fig. 14. The distribution of gage pressure on the reactor section at 600 min.

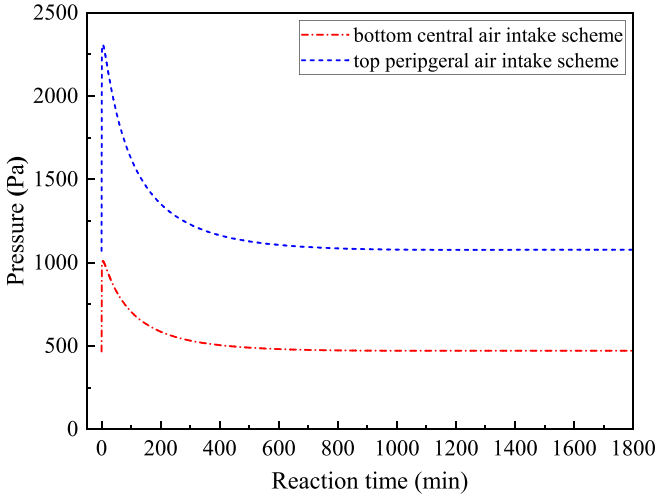

Fig. 15. The average gage pressure at the inlet of reactor over time.

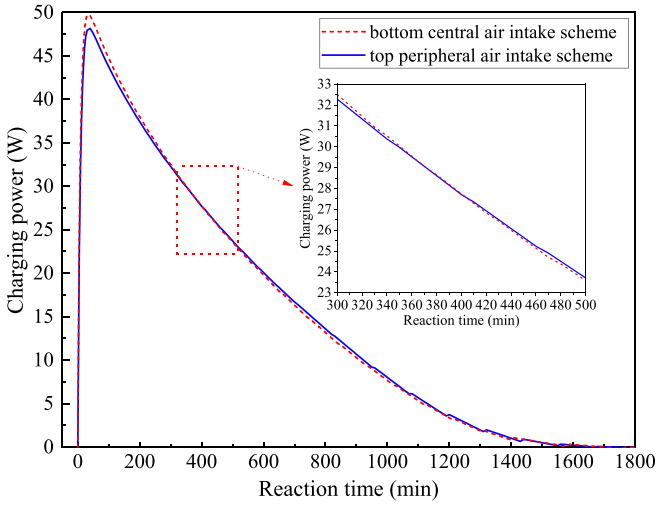

Fig. 16. The average charging power on the salt modules of reactor over time.

dynamics. Fig. 17 shows the changes in the average conversion rate and temperature of the salt modules at different inlet temperatures (75 °C to 95 °C). As the inlet temperature increased, the reaction time decreased. The reaction time was shortened by 46.63 % when the inlet temperature increased from 75 °C to 95 °C, and the heat storage efficiency gradually increased from 80.38 % to 83.77 %. It shows that the increase of inlet air temperature is contribute to increase both the reaction rate and the heat storage efficiency. When the inlet temperature increased by 5 °C, the shortened reaction time was 310.2 min, 234.2 min, 195.8 min and 150.4 min, respectively. It can be seen that the reduction in reaction time decreases gradually after the temperature increases sequentially by the same value.

Fig. 18 shows the variation of the average temperature and conversion rate of each salt module under different inlet velocities. When the velocity increased, the average temperature of the salt module increased at the same time due to the enhanced convective flow in the internal pores of the salt module, which increased the P_{eq} value in formulas (3) and (4), thereby accelerating the reaction kinetics. The reaction time decreased by 20.7 % when the inlet velocity increased from 1 m/s to 3 m/s. The heat storage efficiency increases by only about 0.5 % when the inlet velocity increases by 0.5 m/s. The heat storage efficiency is improved with the reduction of reaction time and heat loss as the velocity increases. The change in the sensible heat storage of the reactor wall and baffles is minimal and almost negligible. It shows that the further increase of the velocity has little effect on the improvement of the reaction kinetics, but it can significantly reduce the reaction time.

In the scope of this study, the relative humidity of the inlet air can be replaced by the partial pressure of water vapor. The range of water vapor partial pressure from 600 Pa to 2500 Pa under normal weather conditions is selected for research, and the corresponding relative humidity range is about 15 % to 60 %. Fig. 19 shows the effect of the partial pressure on the mean bed temperature and conversion. When the partial

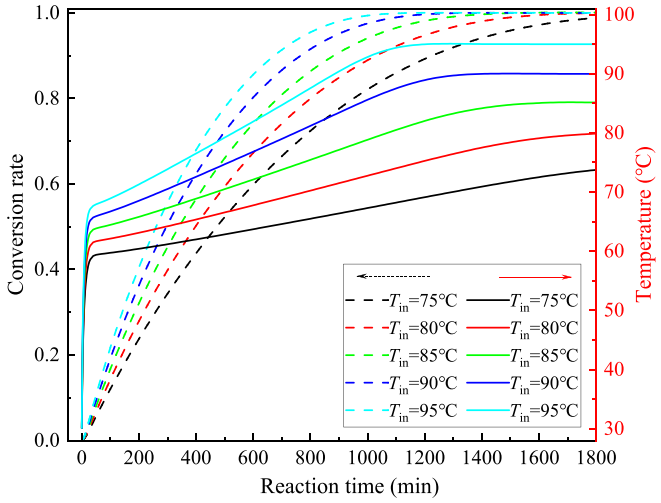

Fig. 17. The average conversion rate and temperature of salt modules with different inlet temperatures.

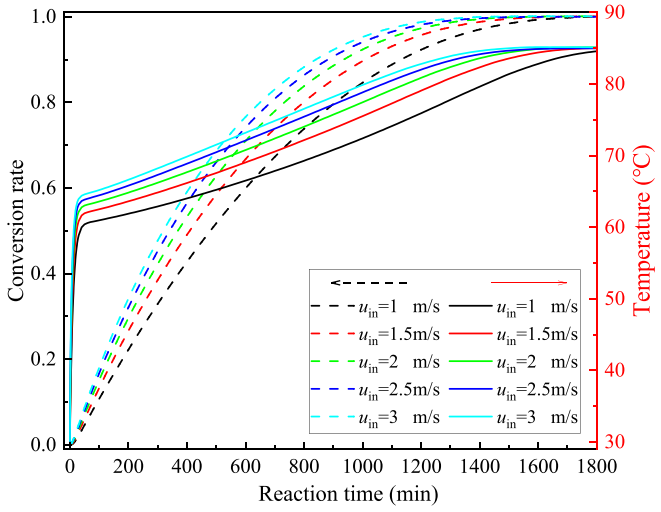

Fig. 18. The average conversion rate and temperature of salt beds with different inlet velocities.

pressure increased from 600 Pa to 2500 Pa, the reaction time increased from 1365.6 min to 1577.3 min with an increase of 15.50 %, while the heat storage efficiency decreased from 82.23 % to 80.04 % with a decrease of 2.66 %. The average temperature of the salt bed increased slightly with increasing partial pressure before ~710 min. The reason is that the reaction rate as well as reaction heat decreases with the increase in P_v. The remaining concentration of hydrated salts is higher when the partial pressure increase which is beneficial for improving the reaction rate after about 710 min. The absorbed reaction heat correspondingly increases which reduces the average temperature of the reaction bed. Therefore, the average temperature slightly decreases with the increase in partial pressure. Table 4 presents the findings regarding the impact of various inlet parameters on the operational performance.

3.2.2. *The influence of spacing between salt modules*

The distance between the salt modules provides a flow channel for the airflow, which increases the contact area between the salt module and the airflow. The size of the spacing affects the flow rate of the airflow as well as the performance of the reactor. Fig. 20 shows the effect of different spacings on the average temperature and conversion rate. The average conversion rate increases when the spacing is decreased

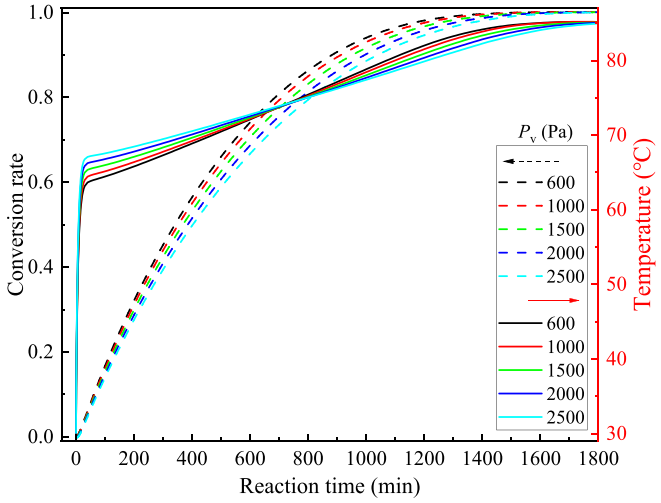

Fig. 19. The average conversion rate and temperature of salt beds with different inlet partial pressures.

from 2 cm to 0.1 cm from Table 5. This is because the air velocity increases as well as the convective heat and mass transfer capacities improve. Heat storage efficiency increased by 10.81 %, and the reaction time was reduced by 16.81 %. It shows that reducing the spacing is beneficial to improving the reaction kinetics and heat storage efficiency. The change rate of the reaction time and heat storage efficiency is nonetheless minor when the spacing continues to drop from 0.3 cm especially as the porosity of the hydrated salt module is small. It is not favorable to the diffusion of water vapor. As a result, the module spacing cannot be <0.3 cm within the design parameters.

3.2.3. *The influence of material properties*

This section mainly studies the effect of porosity and thermal conductivity on charging performance. Porosity has a great influence on the flow resistance and also affect the ESD and thermal efficiency of the system. Fig. 21 shows the average conversion rate and temperature of salt beds with different porosity. The quality of salt reduces as porosity increases, causing a rapid rise in the average temperature and increasing the reaction rate and the conversion rate. The reactive time dropped by 46.36 % from 2079.8 min, the thermal efficiency of heat storage declined by 6.53 % from 85.41 %, and the ESD decreased by 61.5 % as the porosity grew from 0.35 to 0.75.

Fig. 22 delineates the impact of thermal conductivity on the charging process. Notably, as thermal conductivity increases from 0.71 W/(m•K) to 7.1 W/(m•K), there is no significant difference in the average conversion rate or temperature for each salt bed. The curves exhibit only minor discrepancies, which become noticeable after approximately 1400 min into the reaction.

4. Conclusion

A novel multi-module columnar packed-bed open reactor is developed using $SrBr_2$•$6H_2O$ as a TCM in this work. Numerical study is carried out in order to fully utilize the reactor's heat storage performance. The heat storage performance of the two schemes of top peripheral air intake and bottom central air intake is compared, and the influence of different working parameters, structural parameters, and physical parameters on the heat storage performance is studied. The following are the primary conclusions:

(1) Compared with the top peripheral air intake scheme, the bottom central air intake scheme offers advantages such as more uniform reaction rates, shorter reaction times, lower resistance losses, and higher heat storage efficiency.

Table 4
Evaluation results for different indexes on inlet parameters.

Parameter	Variable x_1	Rate of change for x_1	Reaction time (min) x_2	Rate of change for x_2	Thermal efficiency (%) x_3	Rate of change for x_3
Temperature (°C)	75	/	1910	/	80.4	/
	80	6.7 %	1599.8	−16.2 %	81.4	1.2 %
	85	13.3 %	1365.6	−28.5 %	82.2	2.2 %
	90	20.0 %	1169.8	−38.8 %	83.1	3.4 %
	95	26.7 %	1019.4	−46.6 %	83.8	4.2 %
Inlet velocity (m/s)	1	/	1637.9	/	81.2	/
	1.5	50.0 %	1500.7	−8.4 %	81.6	0.5 %
	2	100.0 %	1413.6	−13.7 %	82.0	1.0 %
	2.5	150.0 %	1367.6	−16.5 %	82.2	1.2 %
	3	200.0 %	1299.2	−20.7 %	82.7	1.8 %
Partial pressure (Pa)	600	/	1365.6	/	82.2	/
	1000	66.7 %	1394.8	2.1 %	81.9	−0.4 %
	1500	150.0 %	1462.7	7.1 %	81.2	−1.2 %
	2000	233.3 %	1511.6	10.7 %	80.7	−1.8 %
	2500	316.7 %	1577.3	15.5 %	80.0	−2.7 %

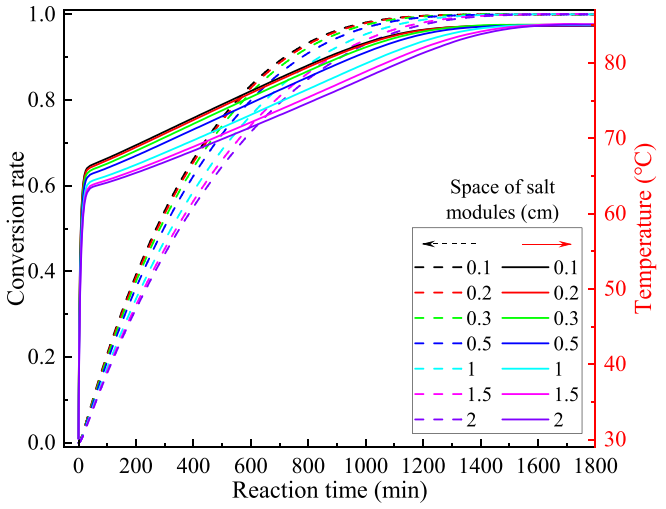

Fig. 20. The average conversion rate and temperature of salt beds with different spaces of salt modules.

(2) Improving the inlet air temperature promotes the reaction process during the charging process. The reaction time is slashed by 46.6 % and the heat storage efficiency is increased by 4.2 % when the inlet temperature rises from 75 to 95 °C.
(3) Further increasing of the velocity has little effect on the improvement of the reaction kinetics, but it can significantly reduce the reaction time. The reaction time decreased by 20.7 % when the inlet velocity increased from 1 to 3 m/s. The heat storage efficiency increases by only about 0.5 % when the inlet velocity increases by 0.5 m/s.
(4) The reaction kinetics are negatively impacted by raising the water vapor partial pressure. The reaction time is increased by

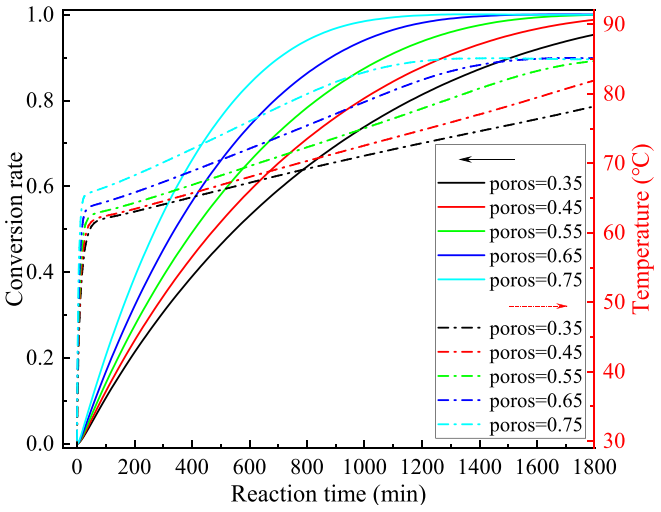

Fig. 21. The average conversion rate and temperature of salt beds with different porosities.

Table 5
Evaluation results for different indexes on structural and physical parameters.

Parameter	Variable ×4	Rate of change for ×4	Reaction time (min) ×5	Rate of change for ×5	Thermal efficiency (%) ×6	Rate of change for ×6
Space of salt modules (cm)	2	/	1392.6	/	80.3	/
	1.5	−25.0 %	1367.6	−1.8 %	82.2	2.4 %
	1	−50.0 %	1301.9	−6.5 %	84.6	5.4 %
	0.5	−75.0 %	1234.3	−11.4 %	87.0	8.3 %
	0.3	−85.0 %	1196.5	−14.1 %	88.0	9.6 %
	0.2	−90.0 %	1166.6	−16.2 %	88.6	10.3 %
	0.1	−95.0 %	1158.5	−16.8 %	89.0	10.8 %
porosity	0.35	/	2079.8	/	85.4	/
	0.45	28.6 %	1893.8	−8.9 %	84.3	−1.3 %
	0.55	57.1 %	1623.3	−21.9 %	83.6	−2.1 %
	0.65	85.7 %	1365.7	−34.3 %	82.2	−3.7 %
	0.75	114.3 %	1115.6	−46.4 %	79.8	−6.6 %
Thermal conductivity (W/(m•K)	0.71	/	1365.7	/	82.2	/
	1.5	111.3 %	1365.7	0.0 %	82.1	−0.1 %
	3.2	350.7 %	1367.6	0.1 %	82.2	0.0 %
	5	604.2 %	1367.6	0.1 %	82.2	0.0 %
	7.1	900.0 %	1367.6	0.1 %	82.2	0.0 %

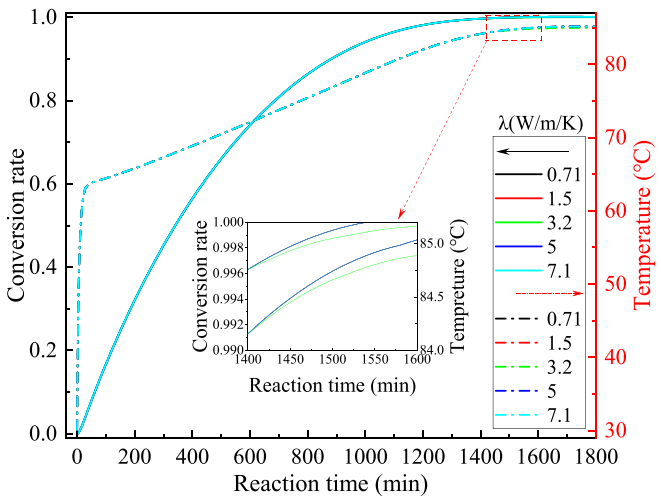

Fig. 22. The average conversion rate and temperature of each salt bed with different thermal conductivities.

15.5 %, and the heat storage efficiency is dropped by 2.7 % as the partial pressure rises from 600 to 2500 Pa.

(5) The reaction time is slashed by 16.8 % and the heat storage efficiency rises by 10.8 % when the spacing between the salt modules is decreased from 2 to 0.3 cm. Further decreasing the spacing from 0.3 to 0.1 cm has little effect on the charging performance. Thus, it is suggested that the spacing of the salt modules be 0.3 cm.

(6) Porosity has a higher impact on reaction times and ESD than that it does on the efficiency of heat storage. The ESD decreases by 61.5 %, the thermal efficiency of heat storage declines by 6.5 %, and the response time decreases by 46.4 % when the porosity increases from 0.35 to 0.75. The effect of thermal conductivity on the efficiency of heat storage is negligible in the circumstances examined in this research.

This research provides a guideline for the design of efficient reactor, promoting the development of thermal chemical energy storage technology.

CRediT authorship contribution statement

Changsheng Hao: System Modelling and Drafting the Manuscript; **Guosheng Feng:** Investigation and Data Curation; **Changjie Ma:** Discussion and Review; **Camila Barreneche:** Discussion and Proofreading; **Xiaohui She:** Conceptualization, Supervision, Funding Acquisition and Revising the Manuscript.

Declaration of competing interest

The authors declare that they have no known competing financial interests or personal relationships that could have appeared to influence the work reported in this paper.

Data availability

Data will be made available on request.

Acknowledgement

This work is supported by the Science and Technology Project of Hebei Education Department (No. BJK2022056) and the Introduction Program of Oversea Talents of Hebei Province (No. C20220505).

References

[1] L. An, T.S. Zhao, Y.S. Li, Carbon-neutral sustainable energy technology: direct ethanol fuel cells, Renew. Sustain. Energy Rev. 50 (2015) 1462–1468.
[2] J. Gasia, D. Groulx, N.H.S. Tay, L.F. Cabeza, Numerical study of dynamic melting enhancement in a latent heat thermal energy storage system, J. Energy Storage 31 (2020) 101664.
[3] J.M. Maldonado, A. de Gracia, L.F. Cabeza, Systematic review on the use of heat pipes in latent heat thermal energy storage tanks, J. Energy Storage 32 (2020) 101733.
[4] I.E. Agency, Net Zero by 2050-a roadmap for the Global Energy Sector, License CC BY 4.0, 2021.
[5] IEA, Global. Energy & CO_2 Status Report 2019, in, 2019.
[6] A. Solé, I. Martorell, L.F. Cabeza, State of the art on gas–solid thermochemical energy storage systems and reactors for building applications, Renew. Sustain. Energy Rev. 47 (2015) 386–398.
[7] R.-J. Clark, A. Mehrabadi, M. Farid, State of the art on salt hydrate thermochemical energy storage systems for use in building applications, J. Energy Storage 27 (2020) 101145.
[8] G. Airò Farulla, M. Cellura, F. Guarino, M. Ferraro, A review of thermochemical energy storage systems for power grid support, Appl. Sci. 10 (2020) 3142.
[9] C. Xu, Z. Yu, Y. Xie, Y. Ren, F. Ye, X. Ju, Study of the hydration behavior of zeolite-$MgSO_4$ composites for long-term heat storage, Appl. Therm. Eng. 129 (2018) 250–259.
[10] P.A.J. Donkers, L.C. Sögütoglu, H.P. Huinink, H.R. Fischer, O.C.G. Adan, A review of salt hydrates for seasonal heat storage in domestic applications, Appl. Energy 199 (2017) 45–68.
[11] H. Mahon, D. O'Connor, D. Friedrich, B. Hughes, A review of thermal energy storage technologies for seasonal loops, Energy 239 (2022) 122207.
[12] J. Xu, T. Li, T. Yan, J. Chao, R. Wang, Dehydration kinetics and thermodynamics of magnesium chloride hexahydrate for thermal energy storage, Sol. Energy Mater. Sol. Cells 219 (2021) 110819.
[13] S. Tae Kim, J. Ryu, Y. Kato, Reactivity enhancement of chemical materials used in packed bed reactor of chemical heat pump, Prog. Nucl. Energy 53 (2011) 1027–1033.
[14] Z.-Q. Dai, Y.-J. Yang, W.-W. Yang, L. Rong, X.-Y. Tang, A thermochemical reactor design with better thermal management and improved performance for methane/carbon dioxide dry reforming, Int. J. Hydrogen Energy 47 (2022) 34794–34809.
[15] A.A. Hawwash, H. Hassan, K.E. Feky, Impact of reactor design on the thermal energy storage of thermochemical materials, Appl. Therm. Eng. 168 (2020) 114776.
[16] W. Li, J.J. Klemeš, Q. Wang, M. Zeng, Salt hydrate–based gas-solid thermochemical energy storage: current progress, challenges, and perspectives, Renew. Sustain. Energy Rev. 154 (2022) 111846.
[17] K. Kant, R. Pitchumani, Advances and opportunities in thermochemical heat storage systems for buildings applications, Appl. Energy 321 (2022) 119299.
[18] W. Li, J.J. Klemeš, Q. Wang, M. Zeng, Numerical analysis on the improved thermochemical behaviour of hierarchical energy materials as a cascaded thermal accumulator, Energy 232 (2021).
[19] A. Cosquillo Mejia, S. Afflerbach, M. Linder, M. Schmidt, Experimental analysis of encapsulated CaO/ca$(OH)_2$ granules as thermochemical storage in a novel moving bed reactor, Appl. Therm. Eng. 169 (2020).
[20] L. Farcot, N. Le Pierrès, J.-F. Fourmigué, Experimental investigation of a moving-bed heat storage thermochemical reactor with $SrBr_2/H_2O$ couple, J. Energy Storage 26 (2019).
[21] M.E. Perez-Davis, F. Difilipo, Energy Storage for a Lunar Base by the Reversible Chemical Reaction: CaO+ H_2O Reversible Reaction ca $(OH)_2$, 1990.
[22] P. Trambouze, J.-P. Euzen, Chemical Reactors: From Design to Operation, Editions OPHRYS, 2004.
[23] A.S. Pujari, R. Majumdar, S.K. Saha, C. Subramaniam, Annular vertical cylindrical thermochemical storage system with innovative flow arrangements for improved heat dispatch towards space heating requirements, Renew. Energy 217 (2023) 119168.
[24] W. Hua, H. Yan, X. Zhang, X. Xu, L. Zhang, Y. Shi, Review of salt hydrates-based thermochemical adsorption thermal storage technologies, J. Energy Storage 56 (2022).
[25] B. Michel, N. Mazet, P. Neveu, Experimental investigation of an open thermochemical process operating with a hydrate salt for thermal storage of solar energy: local reactive bed evolution, Appl. Energy 180 (2016) 234–244.
[26] J. Stengler, M. Linder, Thermal energy storage combined with a temperature boost: An underestimated feature of thermochemical systems, Appl. Energy 262 (2020) 114530.
[27] K. Kant, A. Shukla, D.M.J. Smeulders, C.C.M. Rindt, Performance analysis of a K_2CO_3-based thermochemical energy storage system using a honeycomb structured heat exchanger, J. Energy Storage 38 (2021).
[28] K.E. N'Tsoukpoe, T. Schmidt, H.U. Rammelberg, B.A. Watts, W.K.L. Ruck, A systematic multi-step screening of numerous salt hydrates for low temperature thermochemical energy storage, Appl. Energy 124 (2014) 1–16.
[29] S.C. Costa, M. Kenisarin, A review of metallic materials for latent heat thermal energy storage: Thermophysical properties, applications, and challenges, Renew. Sustain. Energy Rev. 154 (2022) 111812.
[30] F. Desai, J. Sunku Prasad, P. Muthukumar, M.M. Rahman, Thermochemical energy storage system for cooling and process heating applications: a review, Energ. Conver. Manage. 229 (2021) 113617.
[31] T. Esaki, N. Kobayashi, Reaction rate characteristics of SrBr2 hydration system for chemical heat pump cooling mode, J. Mater. Sci. Chem. Eng. 04 (2016) 106–115.

[32] B. Ding, C. Xu, Z. Liao, F. Ye, Study on long-term thermochemical thermal storage performance based on $SrBr_2$-expanded vermiculite composite materials, J. Energy Storage 42 (2021) 103081.
[33] W. Li, H. Guo, M. Zeng, Q. Wang, Performance of $SrBr_2{\cdot}6H_2O$ based seasonal thermochemical heat storage in a novel multilayered sieve reactor, Energ. Conver. Manage. 198 (2019) 111843.
[34] A. Fopah Lele, F. Kuznik, O. Opel, W.K.L. Ruck, Performance analysis of a thermochemical based heat storage as an addition to cogeneration systems, Energ. Conver. Manage. 106 (2015) 1327–1344.
[35] A. Fopah Lele, F. Kuznik, H.U. Rammelberg, T. Schmidt, W.K.L. Ruck, Thermal decomposition kinetic of salt hydrates for heat storage systems, Appl. Energy 154 (2015) 447–458.
[36] A. Malley-Ernewein, S. Lorente, Constructal design of thermochemical energy storage, Int. J. Heat Mass Transf. 130 (2019) 1299–1306.
[37] B. Michel, P. Neveu, N. Mazet, Comparison of closed and open thermochemical processes, for long-term thermal energy storage applications, Energy 72 (2014) 702–716.
[38] Y. Yuan, Y. Li, L. Duan, H. Liu, J. Zhao, Z. Wang, $CaO/ca(OH)_2$ thermochemical heat storage of carbide slag from calcium looping cycles for CO_2 capture, Energ. Conver. Manage. 174 (2018) 8–19.
[39] L. Okhrimenko, J. Dussouillez, K. Johannes, F. Kuznik, Thermodynamic equilibrium and kinetic study of lanthanum chloride heptahydrate dehydration for thermal energy storage, J. Energy Storage 48 (2022) 103562.
[40] A.F. Lele, A Thermochemical Heat Storage System for Households vol. XXIII, SpringerVerlag GmbH, 2016, p. 202.
[41] A.F. Lele, J. Hu, F. Kuznik, T. Osterland, W.K. Ruck, Numerical Investigations OF a Thermochemical Heat Storage System during the Discharging, ResearchgateNet, 2015.
[42] A. Rubino, R.D. Boer, Seasonal storage of solar heat reaction modeling, in: The 10th IIR Gustav Lorentzen Conference on Natural Refrigerants, Delft, The Netherlands 2012, 2012.
[43] C. Ferchaud, H. Zondag, A. Rubino, R. De Boer, Seasonal sorption heat storage-research on thermochemical materials and storage performances, in: Conference; Heat Power Cycle 2012; 2012-09-10; 2012-09-12, ECN, 2012, pp. 1–7.